Morphologicalandmechanicalbiomimeticbonestructures

R.Parwani [1],M.Curto [1],A.P.Kao [1],P.J.Rowley [2],M.Pani [1],G.Tozzi [1],A.H.Barber [1*]

[1] School of Engineering, Anglesea Building, Anglesea Road, University of Portsmouth, Portsmouth PO13DJ,UK.

[2]School ofEarthand Environmental Sciences,Burnaby Building , BurnabyRoad,Universityof Portsmouth, Portsmouth, PO13QL,UK.

Corresponding author: asa.barber@port.ac.uk

Keywords: bone, mechanics, 3D printing, additive manufacturing, x-ray tomography, composites

Abstract

Corticalbone isanexampleofamineralizedtissuecontainingacompositionaldistributionof hard and soft phases in 3-dimensional space for mechanical function. X-ray computed tomography (XCT)isableto describethis compositional and morphological complexity but methods to provide a physical output with sufficient fidelity to provide comparable mechanicalfunction islacking.Aworkflow ispresentedinthisworktoestablishamethod of using high contrast XCT to establish a virtual model of cortical bone that is manufactured usingamultiple materialcapable3Dprinter. Resultant3Dprinted structures wereproduced based on more and lessremodelled bone designsexhibiting a range of secondary osteon density. Variation inresultantmechanicalproperties ofthe3Dprinted composite structures for each bone design was achieved using a combination of material components and reasonable prediction of elasticmodulus provided usingaHashin-Shtrikman approach. The ability to 3D print composite structures using high contrast XCT to distinguish between compositional phasesinabiologicalstructurepromises improved anatomicalmodelsaswell asnext-generationmechano-mimetic implants.

Introduction

Biological processes are adept at producing complex structures optimized for a range of mechanical functions, while maintaining biological function. Such structural complexity requires both morphological and compositional control often lacking in synthetic routes. Bone is a prevalent example of a mineralized tissue demonstrating considerable mechanical performance, including resistance to compression and relatively high toughness [1], by means of optimised combination of hard mineral apatite and a range of softer materials mostly consisting of collagen [2-5]. Bone is commonly classified into a number of hierarchical levels from the whole bone down to nanoscale components [6]. A number of disease states and conditions exist that compromise the mechanical integrity of bone, mainly including osteoporosis and osteoarthritis[7,8]. Considerable improvement in healthcare therefore requires effective replacement of bone material that is able to provide suitable mechanical function.

The replacement of bone broadly follows two pathways of either employing biomaterials for bone tissue engineering to allow bone regeneration [8] or using engineering structures to replace significant volumes of the whole bone via traditional total hip or knee replacements [9]. The former design of biomaterials has become a sophisticated research field that employs a range of solutions that are mostly suited for small defects, whereas larger structures are perhaps less developed [10]. Specifically, prosthetics are typically employed to interface with bone material but lack the morphological and compositional complexity comparable to that of the host material. This lack in complexity often results in failure of the implant, mainly due to aseptic loosening [11].

Manufacturing processes able to provide complexity in order to satisfy mechanical function comparable to bone are limited. Additive layer manufacturing, commonly referred to as three-dimensional (3D) printing, shows significant potential in producing the complexity required for mimicking bone, or indeed any biological structure. Extensive efforts have been made in applying 3D printing to a range of biological structures related areas. Healthcare, particularly in surgery, is an area of significant growth for structures produced from 3D printing[12]. Highlighted use of 3D printing includes the manufacture of anatomic models [13] as

well as surgical guides and templates [14], implants [15] and molds predominantly for maxillofacial and orthopaedic operations [16]. Interestingly, a recent review indicates the activity in 3D printing of anatomic models was over seven times larger than for implant studies [17] and perhaps reflects the demands in controlling the biological and mechanical function of an implant compared to a model. The aim of manufacturing a bone replica mimicking the host tissue using 3D printing therefore remains a significant goal both for providing increasingly effective implants as well as more accurate anatomic models.

Previous works have highlighted the use of 3D printing in presenting engineered structures based on biological composite topologies including a rotated bone-like geometry [18]. 3D printing critically requires a design input that is realised in a physical model output. Such an input ranges from computer aided design (CAD) [13] to more sophisticated use of x-ray computed tomography (XCT) imaging [19]. The latter approach is powerful as the three-dimensional complexity of a biological structure is captured depending on the resolution and field of view. A less developed aspect of XCT scanning resides in capturing both geometric information as well as compositional information based on the attenuation between the probing incident x-ray and the materials organized within the biological structure. The ability to obtain a digital model of bone that maintains high fidelity with the host tissue using XCT is persuasive. While 3D printing shape information from bone has been achieved [20], the use of multiple material 3D printing of biological structures is lacking. Prevalent examples of 3D printed multi-material structures inspired by nature exist for the nacreous layer of seashells that consist of a high volume fraction of hard mineral plates, within soft material referred to as a 'bricks and mortar' organization[21]. The challenge of accurately manufacturing volume fractions above 90% of hard material within a soft matrix material still remains, but works have indicated a broader approach that allows a mimetic hard-soft material composite with functionality that tends towards that of the host biological structure [18]. However, the integration of an efficient workflow that allows information translation from XCT to a virtual model that gives a 3D printed physical output with mechanical fidelity from shape and composition is required. This work presents such an integrated approach demonstrated for compact bone structures. Compact bone is a demanding biological structure for XCT as the solid volume fraction is high, with few voids that provide high contrast at interfaces with the solid mineralised material. Compact bone that is remodelled also gives opportunities to

examine regions of compositional variations between secondary osteons compared to the primary osteonal bulk. The potential for 3D printing structures that retain the characteristics of the host biological tissue additionally require selection of appropriate materials with a distribution of mechanical properties that enables suitable function. While the establishment of a workflow approach from imaging through to manufacturing is critical, the development of future materials is expected to give increased fidelity. A 3D printed structure directly using biological design must finally provide mechanical function comparable to the host to achieve a 'mechano-mimetic' goal.

The main aim of this study is to establish a workflow able to provide a physical 3D printed output of a bone structure using XCT approaches. The resultant structural output is primarily exploiting the power of 3D printing in giving organizational complexity of materials, but utilizes commercially available materials. Materials with a range of mechanical properties will explore the ability to tune composition combined with structural fidelity to approach a more mechano-mimetic 3D printed bone-like structure.

Experimental section

Cortical bone samples were harvested from mature bovines that were bred and slaughtered for alimentary purposes. Typical age of sacrifice in dairy cows ranges 36-48 months and this is considered as the 'biological' age of the samples used in the current study. Samples from the mid-diaphysis of bovine bone femur a were cored by removing cylinders of approximate diameters and lengths of 4mm x 5mm respectively from the host. The long axis of the cored cylinder was parallel to the long axis of the bovine bone femur. Cored samples were extracted from an extensively remodelled bovine bone region showing a significant number of secondary osteons less remodelled bovine bone region limiting the number of secondary osteons. Cored bone samples were wrapped in saline soaked gauze and frozen prior to imaging.

The approach taken here is to image the samples using XCT to give morphological information and identify the compositional variations of primary and secondary bone. Primary bone is produced rapidly in bovine structures but is remodelled into more ordered secondary

osteonal regions. While the composition of bone is predominately hard mineral phase and softer collagen, regions of disordered bone have been shown to have relatively lower stiffness[5] whereas more ordered bone exhibits increased stiffness [22]. A workflow is therefore established as indicated in Figure 1 to image cortical bone samples with regions of compositional variation and then develop a virtual model of the bone, including morphological and mechanical information, which is translated to a 3D printed composite structure of multiple materials exhibiting an organizational fidelity with the host tissue.

Imaging of bone was carried out using an x-ray microscope (Versa 520, Carl Zeiss Ltd., USA) operating with at a 70 kV/6 W X-ray tube energy. A total of 3201 projections across 360 degrees of sample rotation, with each projection collected using a 6 second exposure time provided a 5.3 μm isotropic voxel size. The core samples were immersed in saline during the tomography to prevent desiccation. The 2DX -ray projections from XCT were reconstructed to a 3D volume using a filtered back projection algorithm implemented in the manufacturers software. As tandard Shepp -Logan filter , Gaussian filter (0.5 strength) and beam hardening correction (strength 0.05) was applied to the projections. Approximately 50 slices from the top and bottom regions of the XCT datasets were disregarded due to artefacts. The resulting 3D dataset was segmented into primary and secondary bone regions by thresholding to exclude voxels with a scale of grey value equal to zero .This thresholding allowed provided a 3D analogue of the datasets using image analysis software (Avizo 8, Fra.). An iso surface was extracted from the 3D analogue and triangulated as a mesh of polygons and volume meshes using meshing software (MeshLab v1.3.3., Ita.). Each mesh was decimated in terms of triangles number with a multistep procedure defined by a step number equal to three. A quadric edge collapse decimation algorithm with a quality threshold parameter of 0.5 and a boundary preservation weight of 5 was used to decimate the mesh to reduce data size. Meshes were imported into CAD software (Rhinoceros 5.0, Robert McNeel and Associates, USA) and scaled by x10 to increase feature density within the 3D printed structure . Validation of the closed surface of the meshing and removal of hole artefacts was carried out using software (NetFabb, Autodesk, UK). Finally, 3D printed samples were output ted from the CAD to a physical composite model using a n inkjet based 3D printer (ProJet 5500X, 3D Systems, USA) that allowed the additive deposition of multiple materials. The hardest material was used for the secondary bone regions (VisiJet CR-WT, 3D Systems, USA) and a series of

increasingly softer matrix materials (VisiJet RWT-FBK 100, VisiJet RWT-FBK 250 and VisiJet RWT-FBK 500, 3D Systems, USA) defined as hard, medium and soft respectively were used as the primary bone material. The materials were chosen from the range available commercially for use in the 3D printer. The approximate ratios of the hardest to the increasingly softer materials using the manufacturers elastic modulus specifications are 2.7, 11 and 40 respectively. The ratio of elastic modulus for the secondary osteonal material compared to primary osteon is approximately 10, taken from literature[5], indicating a ratio of 3D printed materials comparable to those found in bone despite the absolute values being lower. These 3D printed base materials are noted as USP Class VI certified for healthcare applications. The printer was operated in XHD mode with a 13 µm spatial resolution is the z-axis and 34 µm spatial resolution in the x- and y- axes of the build plate plane. The long axis of the cortical bone structure was aligned along the x-axis. XCT validation of the 3D printed samples was attempted but was impossible to distinguish between the different material compositions due to similarity of x-ray attenuation across all the base materials.

Mechanical properties of the cortical bone samples and 3D printed mimics were evaluated using acoustic measurements. The propagation of ultrasonic waves is an established method of measuring the elastic properties of bone as well as 3D printed trabecular bone phantoms as demonstrated recently[20]. Samples of bone and 3D printed structures were fixed between a transmitting and receiving transducer setup (Olympus V103/V153, UK). The transducers were clamped using coupling media (ShearGel, Magnaflux, USA) to the opposite ends of the samples using an approximate force of 10 $N.cm^2$ so that the long axis of the sample traversed between the transducers. A 1 MHz sinepulse was generated, with a repetition frequency between 10-1,000 Hz, at the transmitted end of the sample so that the ultrasonic pulse was detected at the receiver using an oscilloscope. The fast first arrival ultrasonic wave velocity, define as the primary p-wave velocity V_p, and secondary s-wave velocity V_s where calculated using:

$$V_p = Lt_p^{-1} \quad (1)$$

$$V_s = Lt_s^{-1} \quad (2)$$

Where t_p and t_s are the p- and s-wave arrival times, and L is the sample length. The apparent elastic modulus E of the cortical bone is calculated from[23]:

$$E = 2\rho V_s^2 \left[1 + \left(\frac{V_p^2 - 2V_s^2}{2(V_p^2 - V_s^2)} \right) \right] \quad (3)$$

Where ρ is the sample density given from volumetric methods.

Results

Complete volumes of the bovine bone were successfully imaged using XCT for both the less remodelled and more remodelled cortical bone samples. Figure 2 shows plane sections orthogonal to the long axis of the bone and indicates the prevalence of the tubular secondary osteon regions in the more remodelled bone and an absence of secondary osteon regions in the less remodelled bone. The 3D tomography data sets for less and more remodelled bone samples were used to provide a virtual model of the bone following a series of steps as shown in Figure 3. The 3D data was segmented to highlight the secondary osteons and then finally meshed with a range of triangular features from approximately 1.5 million for the less remodelled bone to 3 million for the more remodelled bone. The increased digital weight for the more remodelled bone compared to the less remodelled bone was due to the increased number of secondary osteon features in the mesh. The 3D printed physical output from the virtual model is shown in Figure 4 for a number of samples. The 3D printing provides a low density wax material support that is observed as the lighter coloration under the darker structural material.

Mechanical evaluations of the base materials used to construct the 3D printed structures of bovine-like bone are shown in Table 1. Minimal variations of both p- and s- wave velocities between the hardest and hard materials resulted in similar elastic modulus values of 3.95 GPa and 3.85 GPa respectively. A reduction of 16% in elastic modulus is observed between the hard and medium materials with a further 17% reduction in elastic modulus for the soft

material. Elastic modulus measurements for the 3D printed structures and the corresponding less and more remodelled bone samples are shown in Table 2. The bone samples exhibit noticeably higher elastic moduli than the 3D printed structures and is expected to be due to the high elastic modulus, reported as 129 GPa [4], of the mineral phase in bone. Interestingly, the less and more remodelled cortical bone samples have similar elastic moduli. The variation of the secondary osteon composition of the less and more remodelled bone is clearly shown in Figure 2, with analysis of the 3D tomographs indicating volume fractions of 4% and 55 % respectively for less and more remodelled bone. However, the volume fraction porosity of the more remodelled bone is slightly higher at 8% than the 7% for less remodelled bone. The porosity of the less and more remodelled bone samples as well as their corresponding 3D printed designs was taken from the XCT imaging data sets and calculated using volume fraction analysis (VisualSI Advanced, ORS, Can.). The more and less remodelled porosity volume fraction was found to be 7.12% and 6.63% respectively. The corresponding av erage volume fraction porosity from the 3D printed samples for the more and less remodelled designs was 5.47% and 4.24% respectively. The bone samples show a slight increase in porosity from the less to more remodelled bone. The 3D printed samples show the same trend of increasing porosity moving from the less remodelled to the more remodelled bone design. The lower porosity for the 3D printed samples compared to the bone is expected to be due to the meshing process removing small pores that are below the m esh size prior to the 3D printing. We also note that the voxel size of over 5 μm may also ignore sub -micron porosity in bone linked to the larger scale porosity . The increase in the stiffer secondary osteon phase of more remodelled bone is thus potentially offset by the enhanced porosity relative to the less remodelled bone. An attempt to understand the variation in the mechanical properties of the 3D printed structures was attempted by plotting the ratio of hard osteonal -like region to soft matrix against the measured elastic modulus in Figure 5. A linear trend of increasing measured elastic modulus with decreasing ratio was observed for both the less and more remodelled designs. This trend is reasonable as the replacement of a soft matrix with materials of higher elastic modulus, which occurs when moving from the soft to the hard matrix material. The higher volume fraction of osteonal -like material for the more remodelled bone is reflected in the higher elastic modulus of the stru ctures using the corresponding bone design relative to the less remodelled bone design.

Discussion

A workflow providing a manufactured realization of the XCT imaging data has enabled composition and morphology to be captured using multi-material 3D printing. The less and more remodelled bone designs provided morphological information with the selection of a range of base materials providing compositional variation in a 3D printed bone-like structure. While the measured elastic modulus of 3D printed structures are almost ten times smaller than that of the native bone, the potential to increase the elastic modulus of the overall structure is achievable provided higher elastic modulus base materials are used.

An analytical model able to describe the link between the composition of the 3D printed structures and measured elastic modulus, for each cortical bone design, is explored here in order to understand the potential for tuning mechanical properties towards a more mechano-mimetic structure. A Hashin-Shtrikman description of a composite system of softer matrix and harder phase of homogenous, isotropic and arbitrary geometry was considered as appropriate[24]. The elastic modulus of the 3D printed structures was predicted using the generalized form of the Hashin-Shtrikman upper bound for a multiphase composite material[25]. The Hashin-Shtrikman upper bound is expressed in terms of the elastic modulus of the material constituents using:

$$E_{calc} \leq \left[\sum_{i=1}^{N} f_i \left(\frac{E^*_{\max}}{3(1-2\nu)} + \frac{E_i}{3(1-2\nu_i)} \right)^{-1} \right]^{-1} - \frac{E^*_{\max}}{3(1-2\nu)} \qquad (4)$$

Where E_{calc} is the calculated upper bound of the bulk modulus for the composite material, N is the total number of phases in the composite, ϕ_i is the volume fraction of a given phase, E_i the elastic modulus of the individual phase materials, ν is the Poisson's ratio of the given phase measured acoustically[26] and G_{max} is the maximum shear modulus contained within the composite where $E^*_{max}/(1\text{-}2\nu) = 4\,G_{max}$. A plot of the calculated elastic modulus for the Hashin-Shtrikman upper bound condition against the measured elastic modulus from ultrasound measurements are shown in Figure 6 below. The calculated elastic modulus values show somewhat comparable values to the measured elastic modulus values for the 3D printed structures. Further calculations of the elastic modulus for the bone samples using Equation 4

were attempted by incorporating elastic modulus values for the more disordered and ordered collagen structures representative of primary and secondary bone [5] but the resultant correlation with measured elastic modulus values is poor, potentially due to isotropic assumptions in Equation 4 applied to more anistropic constituent behavior in bone . The Hashin-Shtrikman model is limited in predicting the bone elastic modulus but more effective in determining the elastic modulus of the 3D printed composites. The 3D printed materials are amorphous and isotropic, lacking the anisotropy of the materials found in bone such as collagen[1,2]. However, potential geometric features could be incorporated into the printed design to replicate anisotropy but is not considered in this current work. Additionally, the Hashin-Shtrikman model assumes interfaces are elastic and the 3D printed materials are also expected to have strong effective interfaces. Such a statement can be partially justified by th e calculated elastic modulus fitting more closely to the experimentally measured elastic modulus for the 3D printed samples. Bone is known to have weak interfaces [3] and therefore contributes towards a discrepancy between the calculated elastic modulus for the remodelled bone and the experimental measurement. We note that the ultrasonic methods of measuring the elastic modulus of bone tends to give significantly higher results than other mechanical testing techniques [27]. The trend of increasing elastic modulus as stiffer constituents are used is an obvious outcome from Figure 6. The analytical model of Equation 4 is suitable in consistently predicting a higher elastic modulus for the more remodelled bone design across all material compositions compared to the less remodelled bone design. These elastic modulus variations highlights how selecting more appropriate materials, which are currently limited in commercial 3D printing multi-material systems, will achieve both structural and mechanical fidelity with the imaged tissue.

Conclusions

An established workflow that enables the physical output of a 3D printed structure using multiple materials from XCT imaging data has been achieved in this work. Variation in design using less and more remodelled bone samples gave corresponding variability in the elastic modulus of the 3D printed samples and, combined with a range of mechanically diverse materials, allowed selection of a composite structure with an elastic modulus predicted by an upper bound Hashin- Shtrikman model. The ability to 3D print composite structur es from 3D

image data sets is a general approach and can be applied to many biological structures provided sufficient imaging contrast is able to discern morphological features and composition, as well as a suitable range of materials providing fidelity with the native tissue considered. Such success will enable improved 3D printed anatomic models and move towards suitable mechano-mimetic structures for potential next-generation patient specific implants.

Acknowledgements

The authors acknowledge Stephan Gehne for his assistance in acoustic measurements, the Future Technology Centre (FTC) at University of Portsmouth for use of facilities and CDG Ltd. for support in digital facilities.

References

(1) Dunlop, J. W. C.; Fratzl, P. Biological Composites. *Annu. Rev. Mater. Res.* **2010**, *40* (1), 1–24 DOI: 10.1146/annurev-matsci-070909-104421.
(2) Hang, F.; Barber, A. H. Nano-mechanical properties of individual mineralized collagen fibrils from bone tissue. *J. R. Soc. Interface* **2011**, *8*, 500–505 DOI: 10.1098/rsif.2010.0413.
(3) Hang, F.; Gupta, H. S.; Barber, A. H. Nanointerfacial strength between non-collagenous protein and collagen fibrils in antler bone. *J. R. Soc. Interface* **2014**, *11* (92), 20130993 DOI: 10.1098/rsif.2013.0993.
(4) Oyen, M. L.; Ferguson, V. L.; Bembey, A. K.; Bushby, A. J.; Boyde, A. Composite bounds on the elastic modulus of bone. *J. Biomech.* **2008**, *41* (11), 2585–2588.
(5) García-Rodríguez, J.; Martínez-Reina, J. Elastic properties of woven bone: effect of mineral content and collagen fibril orientation. *Biomech. Model. Mechanobiol.* **2016**, 1–14 DOI: 10.1007/s10237-016-0808-z.
(6) Weiner, S.; Wagner, H. D. The Material Bone: Structure-Mechanical Function Relations. *Annu. Rev. Mater. Sci* **1998**, *28*, 271–298.
(7) Madry, H.; van Dijk, C. N.; Mueller-Gerbl, M. The basic science of the subchondral bone. *Knee Surgery, Sport. Traumatol. Arthrosc.* **2010**, *18* (4), 419–433.
(8) Tozzi, G.; De Mori, A.; Oliveira, A.; Roldo, M. Composite hydrogels for bone regeneration. *Materials*. MDPI AG 2016.
(9) Kapadia, B. H.; Berg, R. A.; Daley, J. A.; Fritz, J.; Bhave, A.; Mont, M. A. Periprosthetic joint infection. *Lancet* **2016**, *387*, 386–394 DOI: 10.1016/S0140-6736(14)61798-0.
(10) Arabnejad, S.; Burnett Johnston, R.; Pura, J. A.; Singh, B.; Tanzer, M.; Pasini, D. High-strength porous biomaterials for bone replacement: A strategy to assess the interplay between cell morphology, mechanical properties, bone ingrowth and manufacturing constraints. *Acta Biomater.* **2016**, *30*, 345–356.
(11) Tozzi, G.; Zhang, Q. H.; Tong, J. 3D real-time micromechanical compressive behaviour

of bone-cement interface: Experimental and finite element studies. *J. Biomech.* **2012**, *45*(2), 356 –363.
(12) Provaggi, E.; Leong, J. J. H.; Kalaskar, D. M. Applications of 3D printing in the management of severe spinal conditions. *Proc. Inst. Mech. Eng. H.* **2016** DOI: 10.1177/0954411916667761.
(13) McGurk, M.; Amis, A. A.; Potamianos, P.; Goodger, N. M. Rapid prototyping techniques for anatomical modelling in medicine. *Ann. R. Coll. Surg. Engl.* **1997**, *79* (3), 169 –174.
(14) Malik, H. H.; Darwood, A. R. J.; Shaunak, S.; Kulatilake, P.; El-Hilly, A. A.; Mulki, O.; Baskaradas, A. Three-dimensional printing in surgery: a review of current surgical applications. *J. Surg. Res.* **2015**, *199*(2), 512–522 DOI: 10.1016/j.jss.2015.06.051.
(15) Farré-Guasch, E.; Wolff, J.; Helder, M. N.; Schulten, E. A. J. M.; Forouzanfar, T.; Klein-Nulend, J. Application of Additive Manufacturing in Oral and Maxillofacial Surgery. *J. Oral Maxillofac. Surg.* **2015**, *73*(12), 2408 –2418 DOI: 10.1016/j.joms.2015.04.019.
(16) Arora, A.; Datarkar, A. N.; Borle, R. M.; Rai, A.; Adwani, D. G. Custom-made implant for maxillofacial defects using rapid prototype models. *J. Oral Maxillofac. Surg.* **2013**, *71*(2).
(17) Martelli, N.; Serrano, C.; Van Den Brink, H.; Pineau, J.; Prognon, P.; Borget, I.; El Batti, S. Advantages and disadvantages of 3-dimensional printing in surgery: A systematic review. *Surg.* **2016**, *159*(6), 1485 –1500 DOI: 10.1016/j.surg.2015.12.017.
(18) Dimas, L. S.; Bratzel, G. H.; Eylon, I.; Buehler, M. J. Tough composites inspired by mineralized natural materials: Computation, 3D printing, and testing. *Adv. Funct. Mater.* **2013**, *23*(36), 4629 –4638 DOI: 10.1002/adfm.201300215.
(19) Tellis, B. C.; Szivek, J. A.; Bliss, C. L.; Margolis, D. S.; Vaidyanathan, R. K.; Calvert, P. Trabecular scaffolds created using micro CT guided fused deposition modeling. *Mater. Sci. Eng. C* **2008**, *28*(1), 171 –178 DOI: 10.1016/j.msec.2006.11.010.
(20) Mézière, F.; Juskova, P.; Woittequand, J.; Muller, M.; Bossy, E.; Boistel, R.; Malaquin, L.; Derode, A. Experimental observation of ultrasound fast and slow waves through three-dimensional printed trabecular bone phantoms. *J. Acoust. Soc. Am.* **2016**, *139* (2), EL13-18 DOI: 10.1121/1.4 939297.
(21) Katti, K. S.; Mohanty, B.; Katti, D. R. Nanomechanical properties of nacre. *J. Mater. Res.* **2006**, *21*, 1237 –1242.
(22) Martínez-Reina, J.; Domínguez, J.; García-Aznar, J. M. Effect of porosity and mineral content on the elastic constants of cortical bone: A multiscale approach. *Biomech. Model. Mechanobiol.* **2011**, *10*(3), 309 –322 DOI: 10.1007/s10237- 010-0236-4.
(23) Suggested methods for determining sound velocity. *International Journal of Rock Mechanics and Mining Sciences & Geomechanics Abstracts* . Pergamon 1978, pp 53 – 58.
(24) Hashin, Z.; Shtrikman, S. A variational approach to the theory of the elastic behaviour of multiphase materials. *J. Mech. Phys. Solids* **1963**, *11*(2), 127 –140 DOI: 10.1016/0022-5096(63)90060-7.
(25) Torquato, S.; Yeong, C. L. Y.; Rintoul, M. D.; Milius, D. L.; Aksay, I. A. Elastic properties and structure of interpenetrating boron carbide/aluminum multiphase composites. *J. Amer. Ceram. Soc.* **1999**, *82*, 1263 –1268.
(26) Kumar, A.; Jayakumar, T.; Raj, B.; Ray, K. K. Correlation between ultrasonic shear wave velocity and Poisson's ratio for isotropic solid materials. *Acta Mater.* **2003**, *51* (8), 2417 –2426 DOI: 10.1016/S1359-6454(03)00054- 5.

(27) Grimal, Q.; Haupert, S.; Mitton, D.; Vastel, L.; Laugier, P. Assessment of cortical bone elasticity and strength: Mechanical testing and ultrasound provide complementary data. *Med.Eng.Phys.* **2009**, *31*(9), 1140 –1147.

Figures and Tables

Table 1. List of the p- and s-wave velocities and corresponding calculated elastic modulus values for a range of the 3D printed base materials used.

	P-Wave Velocity ($m.s^{-1}$)	S-Wave Velocity ($m.s^{-1}$)	Density ($g.cm^{-3}$)	Elastic Modulus (GPa)
Hardest	2401	1100	1.19	3.95
Hard	2367	1073	1.22	3.85
Medium	2269	997	1.18	3.24
Soft	2155	921	1.15	2.71

Table 2. List of the p- and s-wave velocities and corresponding calculated elastic modulus values for the less and more remodelled cortical bone samples, and the corresponding 3D printed composite structures with a range of matrix materials.

	P-Wave Velocity ($m.s^{-1}$)	S-Wave Velocity ($m.s^{-1}$)	Density ($g.cm^{-3}$)	Elastic Modulus (GPa)
More remodelled	4591	2104	2.65	32.07
Hard matrix	2409	1101	1.21	4.00
Medium matrix	2331	1070	1.19	3.72
Soft matrix	2290	988	1.18	3.18
Less remodelled	4808	2415	2.04	31.74
Hard matrix	2260	1027	1.20	3.45
Medium matrix	2194	968	1.19	3.08
Soft matrix	2164	910	1.19	2.75

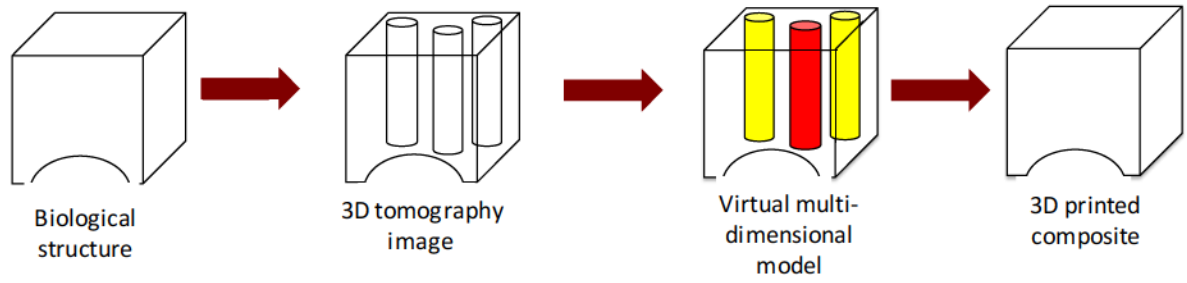

Figure 1. Workflow employed to 3D print a bone structure exhibiting morphological and mechanical fidelity with the host biological structure. XCT is first applied to provide a 3D tomography image of the cortical bone structure. The 3D image data contains both compositional and morphological information that is translated to a virtual multi-dimensional model incorporating morphological information as well as assigning mechanical properties of the primary and secondary osteonal regions. A physical output of this virtual model is provided by the 3D printer.

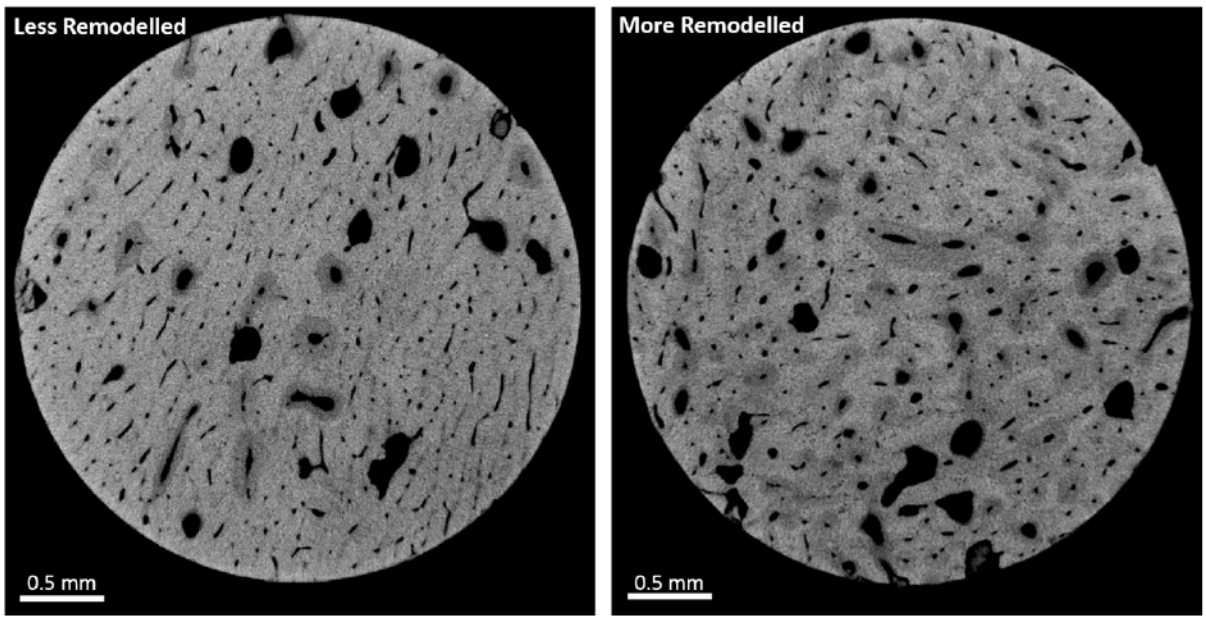

Figure 2. 2D Virtual Slices of the 3D tomography data generated from the XCT highlighting less remodelled (left) and more remodelled (right) cortical bone structure. Extensive secondary osteon regions are shown around the pores of the more remodelled bone whereas more limited numbers of secondary osteon regions are seen in the less remodelled cortical bone.

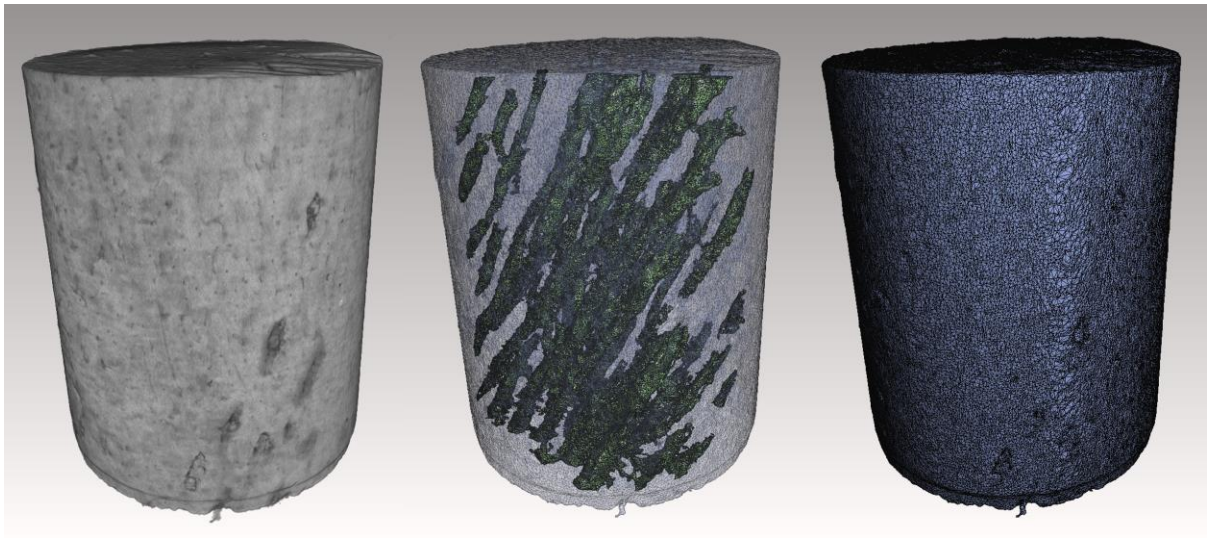

Figure 3. Virtual model development first used the x-ray tomograms (left) and resultant segmented data (middle) to distinguish the primary bone from the tubular features of the secondary osteons. Meshing (right) gave a complete model that was suitable for a physical output from 3D printing that retain compositional and morphological information.

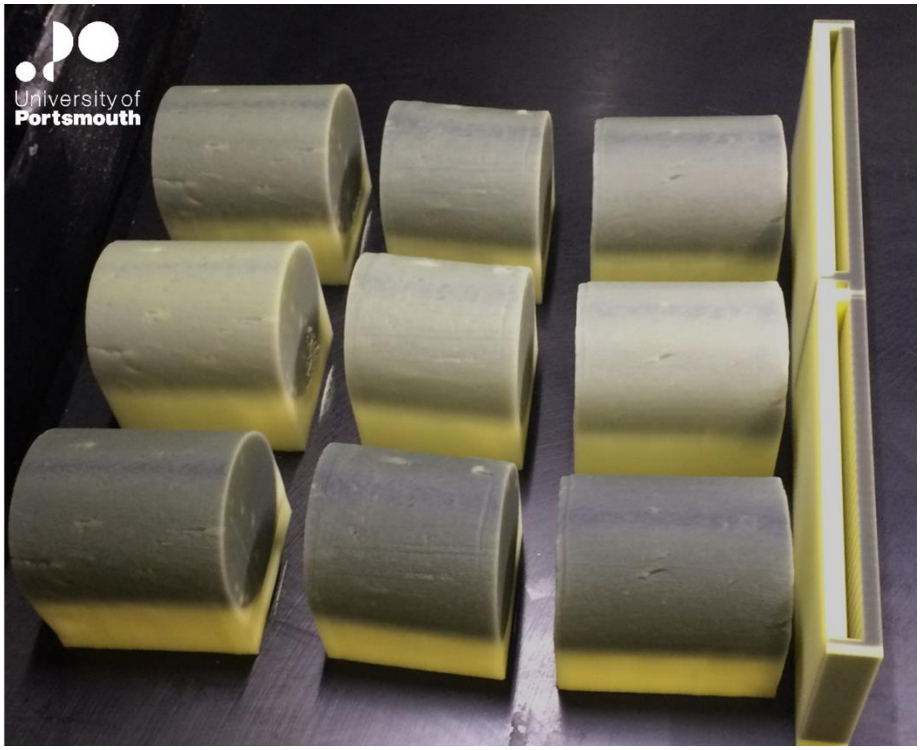

Figure 4. Optical image showing the 3D printing bovine bone structures from XCT data. The printed material is effectively the darker coloration whereas the wax support is the lighter region underneath the sample. Note the long axis of the bone is left to right in the image and parallel to the build plate of the 3D printer.

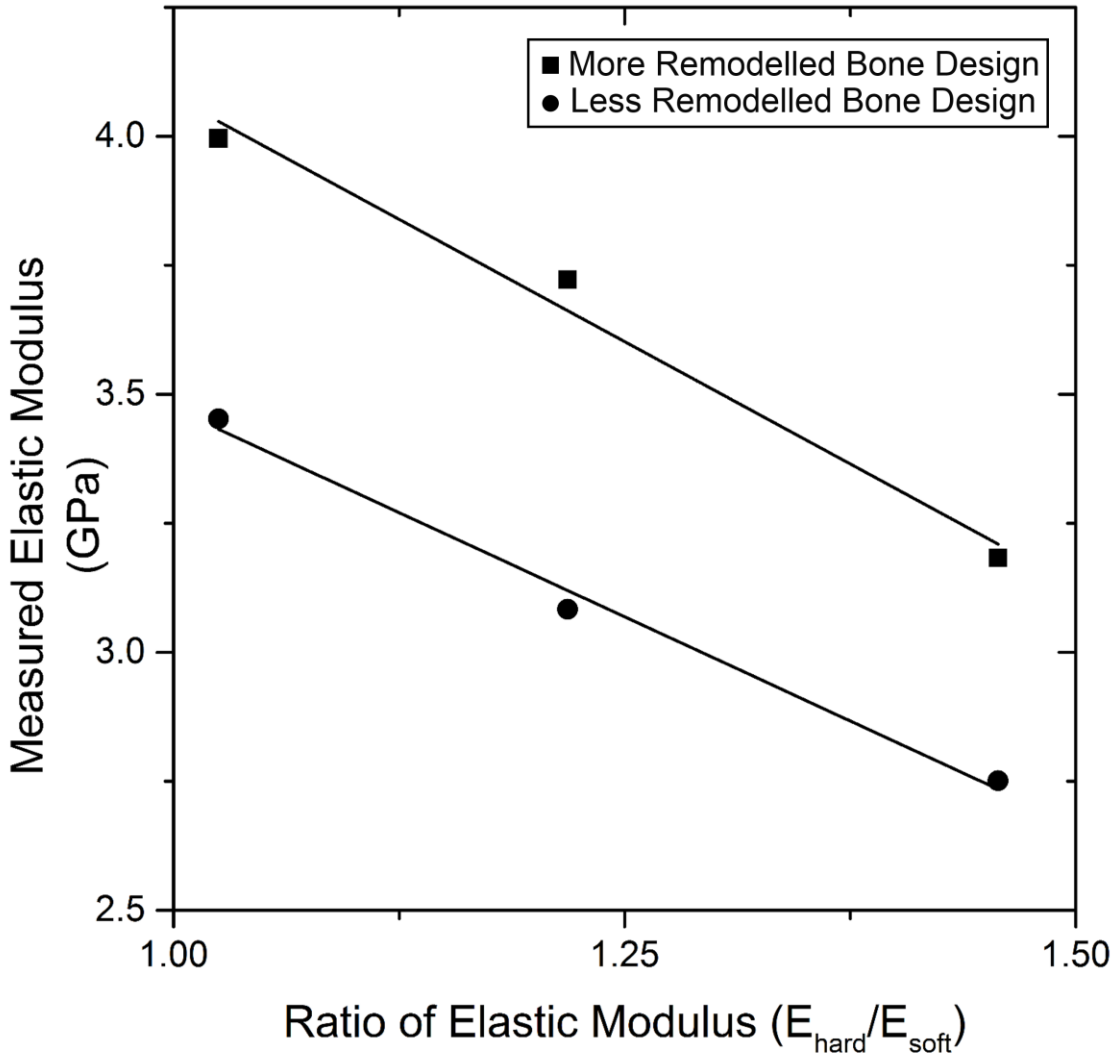

Figure5.Plotofthevariationinthemeasuredelasticmodulusof3Dprintedstructuresbased onlessandmore remodelled corticalbone designwiththeratioofelasticmoduliofthe hard tosoftmaterialsusedinthesestructures.

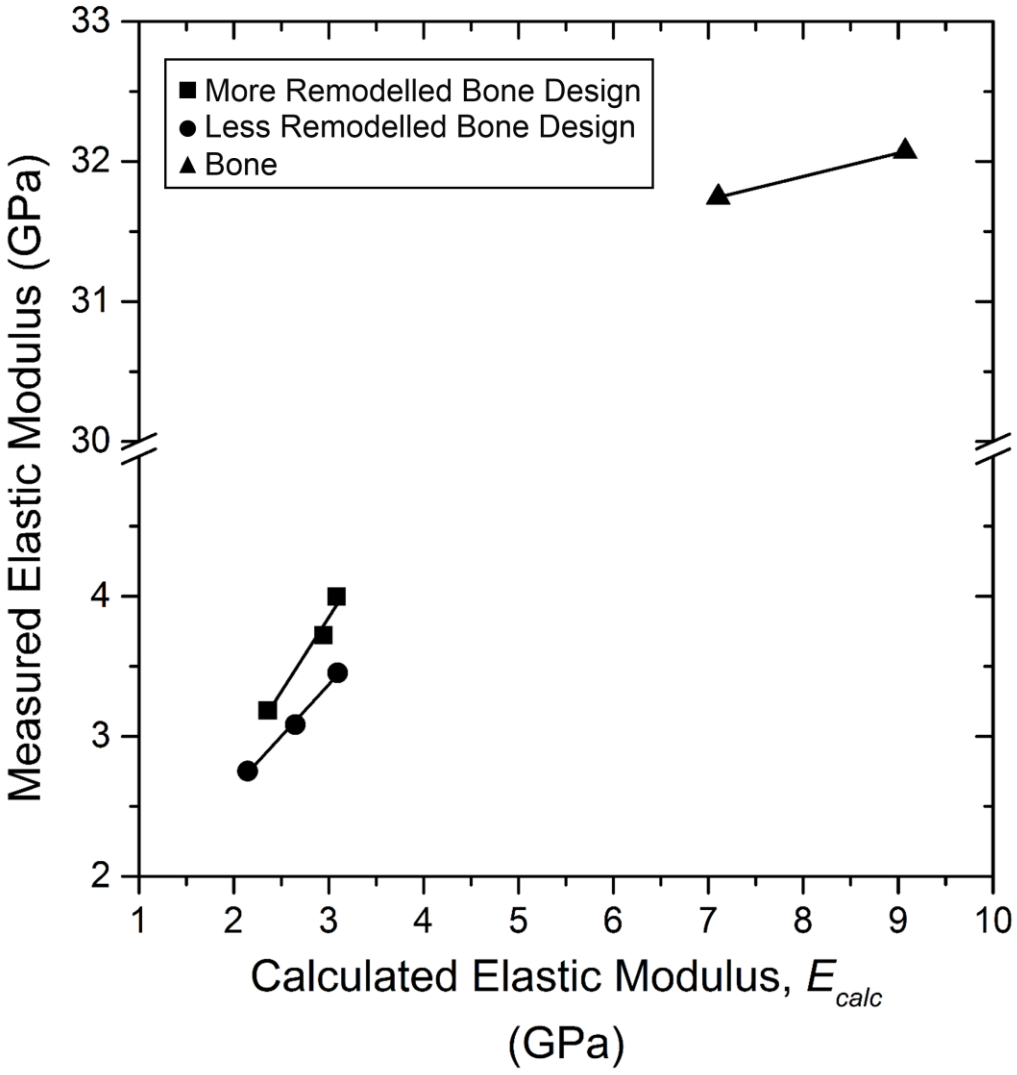

Figure 6. Plot of the measured elastic modulus for bone and 3D printed structures and the corresponding calculated elastic values using the Hashin-Shtrikman upper bound described by Equation 4.

TableofContentsFigure